ATLAS NOTE

ATLAS-CONF-2016-019

31st March 2016

Search for Dark Matter in association with a Higgs boson decaying to b-quarks in pp collisions at $\sqrt{s} = 13$ TeV with the ATLAS detector

The ATLAS Collaboration

Abstract

A search for dark matter pair production in association with a Higgs boson decaying to a pair of bottom quarks is presented, using 3.2 fb^{-1} of pp collisions at a centre-of-mass energy of 13 TeV collected by the ATLAS detector at the LHC. The decay of the Higgs boson is reconstructed as a high-momentum $b\bar{b}$ system with either a pair of small-radius jets, or a single large-radius jet with substructure. The observed data are found to be consistent with the expected backgrounds. Results are interpreted using a simplified model with a Z' gauge boson mediating the interaction between dark matter and the Standard Model as well as a two-Higgs-doublet model containing an additional Z' boson which decays to a Standard Model Higgs boson and a new pseudoscalar Higgs boson, the latter decaying into a pair of dark matter particles.

ATLAS-CONF-2016-019
31 March 2016

1 Introduction

Although dark matter (DM) constitutes the dominant component of matter in the universe, little is known about its properties and particle content [1]. The leading hypothesis suggests that most DM is in the form of stable, electrically neutral, massive particles with cosmological constraints indicating that DM interactions with Standard Model (SM) particles occur at a weak scale or below [2]. Collider-based searches for the particle content of DM provide important complementary information to direct and indirect detection experiments [3].

A traditional dark matter signature at a proton–proton collider is where one or more SM particles, X, are produced and detected, recoiling against missing transverse momentum – with magnitude $E_{\mathrm{T}}^{\mathrm{miss}}$– associated with the non-interacting DM candidate. A number of searches at the Large Hadron Collider (LHC) [4] have been performed recently, where X is considered to be a hadronic jet [5, 6], b or t quarks [7–9], a photon [10–13], or a W/Z boson [14–17]. The discovery of a Higgs boson, h [18, 19], provides a new opportunity to search for DM production via the $h + E_{\mathrm{T}}^{\mathrm{miss}}$ signature [20, 21]. In contrast to most of the aforementioned probes, Higgs boson radiation from an initial-state quark is Yukawa-suppressed. As a result, in a potential signal the Higgs boson would be part of the interaction producing the DM, providing unique insight into the structure of the DM coupling to SM particles. Recently, the ATLAS Collaboration has published such searches using 20.3 fb^{-1} of proton–proton collision data at $\sqrt{s} = 8$ TeV, exploiting the Higgs boson decays to two photons and a pair of bottom quarks [22, 23].

This paper presents an update on the search for $h + E_{\mathrm{T}}^{\mathrm{miss}}$, where the Higgs boson decays to a pair of bottom quarks ($h \to b\bar{b}$), using 3.2 fb^{-1} of pp collision data collected by the ATLAS detector at the centre-of-mass energy of 13 TeV during 2015. The results are interpreted in the context of simplified models of DM, characterized by a minimal particle content and the corresponding renormalizable interactions [24].

Many simplified models of DM production contain a massive particle which can be a vector, an axial-vector, a scalar or a pseudoscalar and mediates the interaction between DM and the Standard Model. In this search, simplified models involving a vector mediator are considered following the recommendations of the recommendation in Ref. [25].

In the first model [20], a vector mediator, Z', is exchanged in the $s-$channel, radiates the Higgs boson and decays into two DM particles. A Feynman diagram for this process is shown in Figure 1(a). The vector mediator is associated to the baryon number B, which is assumed to be gauge invariant under $U(1)_B$ thus allowing it to couple to quarks [26]. This symmetry is spontaneously broken to generate the Z' mass. However, there is no Z' coupling to leptons as such couplings are tightly constrained by dilepton searches. Finally, the dark matter candidate carries a baryon number, which allows it to couple to quarks through the Z'. The parameters of this model are as follows: the coupling of Z' to dark matter (g_χ), the coupling of Z' to quarks (g_{q}), the coupling of Z' to the SM Higgs boson ($g_{Z'}$), the mixing angle between the baryonic Higgs boson, introduced in the model to generate the Z' mass, and the SM Higgs boson ($\sin\theta$), the Z'mass ($m_{Z'}$), and the DM mass (m_χ).

In the second model, apart from the vector mediator, the SM is extended by an additional Higgs field doublet. In this two-Higgs-doublet model (2HDM) five physical Higgs bosons [21] appear: a light scalar h associated with the observed Higgs boson, a heavy scalar H, a pseudoscalar, A, and two charged scalars $H^{\pm}$. The vector mediator is produced resonantly and decays as $Z' \to hA$, in a Type-II two-Higgs-doublet model [27]. The pseudoscalar A subsequently decays into two DM particles with a large branching ratio. A Feynman diagram for this process is shown in Figure 1(b). To fully define the model, the ratio of the up and down type vacuum expectation values, $\tan\beta$, must be specified along with the Z' gauge coupling,

g_Z, and the dark matter mass, m_χ. The results presented are for the alignment limit, in which the $h - H$ mixing angle α is related to β by $\alpha = \beta - \pi/2$. Only regions of parameter space consistent with precision electroweak constraints [28] and with constraints from direct searches for dijet resonances [29–31] are considered. As the A boson is produced on-shell and decays into DM, the mass of the DM particle does not affect the kinematic properties or cross-section of the signal process when it is below half of the A boson mass. Hence, the Z'-2HDM model is interpreted in the parameter spaces of Z' mass ($m_{Z'}$), A mass (m_A) and $\tan\beta$.

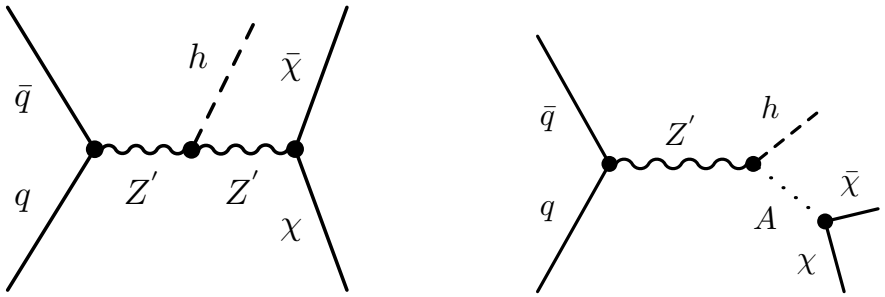

(a) (b)

Figure 1: Feynman diagrams showing (a) the simplified models where a Z' decays to a pair of DM candidates $\chi\bar{\chi}$ after emitting a Higgs boson h, and where (b) a Z' decays to a Higgs boson h and the pseudoscalar A of a two Higgs-doublet model, and the latter decays to a pair of DM candidates $\chi\bar{\chi}$.

2 ATLAS detector

ATLAS is a multi-purpose particle physics experiment [32] at the LHC, with an approximately forward-backward symmetric and hermetic cylindrical geometry[1]. At its inner-most part lies the inner detector (ID), immersed in a 2 T axial magnetic field provided by a thin superconducting solenoid, consisting of silicon pixel and microstrip detectors, providing precision tracking in the pseudorapidityrange $|\eta| < 2.5$. It is complemented by a transition radiation tracker providing tracking and particle identification information for $|\eta| < 2.0$. Between Run 1 and Run 2 of the LHC, the pixel detector was upgraded by the addition of a new innermost layer [33] that significantly improves the identification of heavy flavour jets [34, 35]. The solenoid is surrounded by sampling calorimeters: a lead/liquid-argon (LAr) electromagnetic calorimeter for $|\eta| < 3.2$ and a steel/scintillating tile hadronic calorimeter for $|\eta| < 1.7$. Additional LAr calorimeters with copper and tungsten absorbers provide coverage up to $|\eta| = 4.9$. At the outer-most part, air-core toroids provide the magnetic field for the muon spectrometer. The latter consists of three stations of gaseous detectors, monitored drift tubes and cathode strip chambers for muon identification and momentum measurements for $|\eta| < 2.7$, and resistive plate and thin-gap chambers for triggering up to $|\eta| = 2.4$. A two-level trigger system, custom hardware followed by a software-based level, is used to reduce the event rate to about 1 kHz for offline storage.

[1] ATLAS uses a right-handed coordinate system with its origin at the nominal interaction point (IP) in the center of the detector and the z-axis along the beam pipe. The x-axis points towards the centre of the LHC ring, and the y-axis points upwards. Cylindrical coordinates (r, ϕ) are used in the transverse plane, ϕ is the azimuthal angle around the beam pipe. The pseudorapidity η is defined as $\eta = -\ln[\tan(\theta/2)]$, where θ is the polar angle.

3 Data and simulation samples

The data sample used in this search, collected during normal operation of the detector, corresponds to an integrated luminosity of 3.2 fb^{-1}. The primary data sample is selected using a calorimeter based $E_{\mathrm{T}}^{\mathrm{miss}}$ trigger, with a threshold of 70 GeV. The trigger efficiency for signal events selected by the offline analysis is about 90% for events with $E_{\mathrm{T}}^{\mathrm{miss}}$ of 150 GeV and reaches 100% for events with $E_{\mathrm{T}}^{\mathrm{miss}}$ larger than 200 GeV.

Signal samples are generated with MadGraph5_aMC@NLO v2.2.3 [36], interfaced to Pythia8.186 using the NNPDF2.3 parton distribution functions (PDF) set [37] and the A14 parameter tune [38] for parton showering, hadronization, underlying event simulation, and for simulation of the Higgs boson decay to a pair of bottom quarks. For the vector-mediator simplified models, signals are generated with mediator mass between 10 and 2000 GeV and DM mass between 1 and 1000 GeV. The event kinematics are largely independent of the other parameters of the model, and thus the same values of these parameters, chosen following the recommendations in Ref. [25]: $g_\chi = 1.0$, $g_{\mathrm{q}} = 1/3$, $g_{Z'} = m_{Z'}$, $\sin\theta = 0.3$. For the Z'-2HDM model, $pp \to Z' \to Ah \to \chi\bar{\chi}h$ samples are produced with Z' mass values between 600 and 1000 GeV, A mass values between 300 and 800 GeV (where kinematically allowed), and a DM mass value of 100 GeV. The other parameters chosen for this model are taken to be $\tan\beta = 1.0$ and $g_Z = 0.8$.

Higgs boson production in association with a W or Z vector boson, Vh, is modelled using Pythia8.186. with NNPDF2.3. The samples are normalised to the SM total cross-sections calculated at next-to-leading order (NLO) [39] and next-to-next-to-leading order (NNLO) [40] in QCD for Wh and Zh, respectively, and include NLO electroweak corrections [41]. In all cases, the Higgs boson mass is set to 125 GeV.

Simulated samples of vector boson production in association with jets, W/Z+jets, where the W or Z boson decay in all leptonic decay modes, are generated using SHERPA 2.1.1 [42], including b- and c-quark mass effects, and the CT10 PDF set [43]. Matrix elements are calculated for up to two partons at NLO and four partons at LO using the Comix [44] and OpenLoops [45] matrix element generators and merged with the SHERPA parton shower [46] using the ME+PS@NLO prescription [47]. The cross-sections are determined at NNLO [48] in QCD. Furthermore, these backgrounds are split into different components according to the true flavour of the two jets that are used to reconstruct the Higgs boson: l denotes a light quark (u, d, s) or a gluon and the heavy quarks are denoted by c and b. This division is performed to allow for accurate modelling of the W/Z+ heavy flavour backgrounds in the combined fit described in Section 8.

The $t\bar{t}$ and single top-quark backgrounds are generated with POWHEG-BOX [49] using the CT10 PDF set. It is interfaced with Pythia6.428 [50] for simulating parton showering, fragmentation, and the underlying event, for which CTEQ6L1 PDF set [51] and the Perugia 2012 parameter tune [52] are used. The $t\bar{t}$ cross-section is determined at NNLO in QCD and next-to-next-to-leading logarithms (NNLL) for soft gluon radiation [53], while the single top-quark cross-sections are fixed to those in Ref. [54–56]. A top quark mass of 172.5 GeV is used throughout.

Diboson production modes, including ZZ, WW, and WZ processes, with one boson decaying hadronically and the other leptonically are simulated using the SHERPA 2.1.1 generator with the CT10 PDF set. They are calculated for up to one (ZZ) or zero (WW/WZ) additional partons at NLO and up to three additional partons at LO using the Comix and OpenLoops matrix element generators and merged with the SHERPA parton shower using the ME+PS@NLO prescription. Their cross-sections are determined by the generator at NLO.

The simulated samples are processed with the detailed ATLAS detector simulation [57] based on GEANT4 [58]. Effects of multiple proton–proton interactions (pileup) as a function of the instantaneous luminosity are taken into account by overlaying simulated minimum-bias events generated with PYTHIA8.186 [59] with the A2 tune [60] and MSTW2008LO parton distribution functions (PDF) [61] onto the hard-scattering process, such that the distribution of the average number of interactions per bunch crossing in the simulated samples matches that in the data.

4 Object reconstruction

Proton–proton collision vertices are reconstructed using ID tracks with $p_{\mathrm{T}} > 0.4$ GeV. The primary vertex is defined as the vertex with the highest $\Sigma(p_{\mathrm{T}}^{\mathrm{track}})^2$, where $p_{\mathrm{T}}^{\mathrm{track}}$ refers to the transverse momentum of each track. Each event is required to have at least one vertex reconstructed from at least two tracks.

Muon candidates are identified by matching tracks found in the ID to either full tracks or track segments reconstructed in the muon spectrometer, and are required to satisfy the "*loose*" muon identification quality criteria [62]. Electron candidates are identified as ID tracks that are matched to a cluster of energy in the electromagnetic calorimeter. Electron candidates must satisfy a likelihood-based identification criterion [63] based on shower shape and track selection criteria, and are selected using the "*loose*" working point. Both muons and electrons are required to originate from the primary vertex, to have $p_{\mathrm{T}} > 7$ GeV, and to lie within $|\eta| < 2.5$ for muons and $|\eta| < 2.47$ for electrons. They are further required to be isolated using requirements on the sum of p_{T} of the tracks within a cone around the lepton direction. The cone size and the requirements are varied as a function of the lepton p_{T}.

Jets are reconstructed in two categories, small-radius (small-R) and large-radius (large-R) jets. In both cases, the jets are reconstructed from topological clusters of calorimeter cells using the anti-k_t jet clustering algorithm [64]. In the case of small-R jets, a radius parameter of $R = 0.4$ is used and the effects of pileup are corrected for by a technique based on jet area [65]. In the case of large-R jets, a radius parameter of $R = 1.0$ is used and the jet trimming algorithm [66] is applied to minimize the impact of energy depositions due to pileup and the underlying event. This algorithm reconstructs subjets within the large-R jet using the k_{t} algorithm [67] with radius parameter $R_{\mathrm{sub}} = 0.2$ and removes any subjet with p_{T} less than 5% of the large-R jet p_{T}. The jet energy scale, and also in the case of large-R jets the jet mass scale, is calibrated to the particle level on average using p_{T}- and η-dependent factors determined from simulation, with small-R jets receiving further calibrations using *in situ* measurements [68]. Small-R jets within the ID acceptance, $|\eta| < 2.5$, are called in the following *central* and are required to satisfy $p_{\mathrm{T}} > 20$ GeV. Those with $2.5 < |\eta| < 4.5$ are called *forward* and are required to satisfy $p_{\mathrm{T}} > 30$ GeV. For small-R jets with $p_{\mathrm{T}} < 50$ GeV and $|\eta| < 2.5$, to reduce the effects of pileup, a significant fraction of the tracks associated with each jet must have an origin compatible with the primary vertex, as defined by the jet vertex tagger [69]. Furthermore, small-R jets are removed if they are within $\Delta R < 0.2$ of an electron candidate. Large-R jets are required to satisfy $p_{\mathrm{T}} > 250$ GeV and $|\eta| < 2.0$, and the highest p_{T} large-R jet invariant mass is used as the final discriminant.

Track-jets are built from tracks using the anti-k_t algorithm with $R = 0.2$. Track-jets with $p_{\mathrm{T}} > 10$ GeV and $|\eta| < 2.5$ are selected and are ghost-associated [70] to large-R jets. Small-R jets and track-jets containing b-hadrons are identified – "b-tagged" – using a boosted decision tree that combines information on the impact parameter and reconstructed secondary vertices of the tracks associated with these jets [34, 35, 71]. A configuration is used which achieves an average efficiency of 70% in identifying small-R (track) jets containing a b-hadron with misidentification probabilities of $\sim 12(18)\%$ for charm-quark jets and

$\sim 0.2(0.6)\%$ for light-flavour jets, as determined in a simulated sample of $t\bar{t}$ events. Track jets have higher misidentification probabilities due to the smaller radius parameter used.

The missing transverse momentum, $\vec{E}_{\mathrm{T}}^{\mathrm{miss}}$, is defined as the negative vector sum of the transverse momenta of the calibrated physics objects – electrons, muons, small-R jets – with unassociated energy depositions, referred to as the soft-term, accounted for using ID tracks of at least 0.5 GeV [72, 73]. Furthermore, a track-based missing transverse momentum vector, $\vec{p}_{\mathrm{T}}^{\mathrm{miss}}$, is calculated as the negative vector sum of the transverse momenta of tracks with $|\eta| < 2.5$, consistent with originating from the primary vertex. [2]

5 Event selection

For an event to be considered in the search, it is required to have $E_{\mathrm{T}}^{\mathrm{miss}} > 150$ GeV, $p_{\mathrm{T}}^{\mathrm{miss}} > 30$ GeV, and no identified, isolated muons or electrons. This is also referred to as *zero-lepton region*.

Events with $E_{\mathrm{T}}^{\mathrm{miss}}$ less than 500 GeV are considered in the *resolved region*. First, this set of events is required to have at least two central small-R jets. Following this selection, the reconstructed small-R jets are ranked as follows. First, the central jets are divided into two categories, those that are b-tagged and those that are not. Each of these samples of jets are ordered in decreasing p_{T}. The ordered set of b-tagged jets is considered with the highest priority, while those that are central but not b-tagged are considered with second priority, and finally any forward jets, ordered in decreasing p_{T}, are considered last. The two most highly ranked jets are used to reconstruct the Higgs boson candidate, h_{r}, and therefore cannot contain forward jets. Furthermore, it is required that at least one of the jets constituting h_{r} should satisfy $p_{\mathrm{T}} > 45$ GeV. To achieve a high $E_{\mathrm{T}}^{\mathrm{miss}}$ trigger efficiency, events are retained if the scalar sum of the p_{T} of the three leading jets is greater than 150 GeV. This requirement is lowered to 120 GeV if only two central small-R jets are present.

Additional selections are applied to suppress further the multijet background. Specifically, to reject events with $E_{\mathrm{T}}^{\mathrm{miss}}$ due to mismeasured jets a requirement is applied on the minimum azimuthal angle between the direction of the $E_{\mathrm{T}}^{\mathrm{miss}}$ and the jets, $\min\left(\Delta\phi\left(\vec{E}_{\mathrm{T}}^{\mathrm{miss}}, \mathrm{jets}\right)\right) > 20°$, for the three highest-ranked jets. Furthermore, the azimuthal angle between the $\vec{E}_{\mathrm{T}}^{\mathrm{miss}}$ and the $\vec{p}_{\mathrm{T}}^{\mathrm{miss}}$, $\Delta\phi\left(\vec{E}_{\mathrm{T}}^{\mathrm{miss}}, \vec{p}_{\mathrm{T}}^{\mathrm{miss}}\right)$, is required to be less than 90°, to suppress events with misreconstructed missing transverse energy. The Higgs boson candidate is required to be well separated in azimuth from the missing transverse momentum by requiring $\Delta\phi\left(\vec{E}_{\mathrm{T}}^{\mathrm{miss}}, h_{\mathrm{r}}\right) > 120°$. Finally, to reject back-to-back dijet production, the azimuthal opening angle of the two jets forming the Higgs boson candidate is required to be $\Delta\phi\left(j_{h_{\mathrm{r}}}^{1}, j_{h_{\mathrm{r}}}^{2}\right) < 140°$.

Because the DM signal is expected to have large $E_{\mathrm{T}}^{\mathrm{miss}}$, whereas the amount of background is expected to be most prominent at low $E_{\mathrm{T}}^{\mathrm{miss}}$, to preserve the increased sensitivity of the high $E_{\mathrm{T}}^{\mathrm{miss}}$ region, events in the resolved region in three categories based on the reconstructed $E_{\mathrm{T}}^{\mathrm{miss}}$: 150 – 200 GeV, 200 – 350 GeV, and 350 – 500 GeV.

In the *merged region* – comprised of events with $E_{\mathrm{T}}^{\mathrm{miss}}$ in excess of 500 GeV – the presence of at least one large-R jet is required, associated with at least two track-jets [74]. In an analogous way to the resolved region, the events are classified based on the number of b-tagged track-jets associated with the large-R jet into three categories with 0, 1, and 2 b-tags.

[2] Throughout this search, the magnitude of $\vec{E}_{\mathrm{T}}^{\mathrm{miss}}$ is referred to as MET and the magnitude of $\vec{p}_{\mathrm{T}}^{\mathrm{miss}}$ is referred to as $p_{\mathrm{T}}^{\mathrm{miss}}$. Only when the directionality is necessary does the notation use the vector symbol.

The search is performed by implementing a shape fit of the reconstructed dijet mass (m_{jj}) or single large-R jet mass (m_J) distribution. After event selection, the energy calibration of the b-tagged jets is improved as follows. The invariant mass of the candidate is corrected [75] in case a muon is identified within $\Delta R < 0.4$ of a b-tagged small-R jet, or within $\Delta R < 1.0$ of the large-R jet. The four-momentum from the closest muon in ΔR within a jet is added to the calorimeter-based jet energy after removing the energy deposited by the muon in the calorimeter (muon-in-jet correction). Additionally, a simulation-based jet p_{T}-dependent correction [75] is applied in the case of b-tagged small-R jets to improve the signal resolution of the reconstructed Higgs mass peak. Events consistent with a DM signal will have a reconstructed mass near the Higgs boson mass, thereby allowing the sidebands to act as a natural control region to further constrain the backgrounds in addition to the dedicated W/Z + jets and $t\bar{t}$ control regions and the multijet estimates described in Section 6.

6 Background estimation

The background is dominantly composed of SM W/Z+jets and $t\bar{t}$ backgrounds, which constitutes 15–65% and 45–80% of the total background, respectively, depending on the $E_{\mathrm{T}}^{\mathrm{miss}}$ value. The model for these backgrounds is constrained using two dedicated control regions. Other backgrounds, including diboson, Vh, and single top-quark production, constitutes less than 15% of the total background and the estimation is modeled using simulated samples. The contribution from multijet events arises mainly from events containing jets with semi-muonic decays. It constitutes less than 2% of the background in the resolved region and negligibly small in the merged region and is estimated using a data-driven technique.

In addition to the zero lepton region, which serves as a control region to constrain the Z + jets background in the zero b-tag case and via the reconstructed mass sidebands, two dedicated control regions, targeted at constraining the main W/Z + jets and $t\bar{t}$ backgrounds are used. These control regions are defined based on the number of leptons and b-tags in the event and are orthogonal to each other and to the signal region.

The *one-muon control region* is designed to constrain the W + jets and $t\bar{t}$ backgrounds. Events are selected using the $E_{\mathrm{T}}^{\mathrm{miss}}$ trigger and are required to have exactly one muon candidate. Furthermore, the full signal region selection is applied after modifying the $E_{\mathrm{T}}^{\mathrm{miss}}$ observable to mimic the behavior of such events that contaminate the signal region by not considering the muon in the $E_{\mathrm{T}}^{\mathrm{miss}}$ calculation. As in the signal region, these events are divided into exclusive regions of the number of b-tags. This division naturally separates $t\bar{t}$ from W + jet events.

The *two-lepton control region* is used to constrain the Z + jets background contribution. Events are collected using a single electron or single muon trigger and selected by requiring exactly one pair of same-flavour electrons or muons. Of these two leptons, one is required to have $p_{\mathrm{T}} > 25$ GeV. The electron (muon) pair must have an invariant mass $83 < m_{\ell\ell} < 99$ GeV ($71 < m_{\ell\ell} < 106$ GeV). In the muon channel, where a larger mass window is used, an opposite charge requirement is also applied. Furthermore, the missing transverse energy significance, defined as the ratio of $E_{\mathrm{T}}^{\mathrm{miss}}$ to the square root of the scalar sum of lepton and jet p_{T} in the event, is required to be less than 3.5 in order to reject $t\bar{t}$ background. In this control region, the transverse momentum of the dilepton system, p_{T}^{V} is used - instead of $E_{\mathrm{T}}^{\mathrm{miss}}$- to match the division of the resolved and merged regions and the categorisation of the resolved events. Other than the above, the event selection and Higgs boson candidate requirements are the same as in the signal region.

The multijet background for the resolved analysis is determined using a data-driven method. A sample of events selected to satisfy the analysis trigger, $p_{\mathrm{T}}^{\mathrm{miss}}$ requirement, and inverting the $\min(\Delta\phi(\vec{E}_{\mathrm{T}}^{\mathrm{miss}}, \mathrm{jets}))$ requirement, is used to provide multijet templates of all the distributions relevant to the analysis. These templates are normalised by a fit to the distribution of the number of small-R jets that contain a muon in the nominal selection. The fit is performed separately for each b-tag category. Since agreement is found between the categories the average normalisation scale factor is used. In the merged region, it was found that the requirement of high $E_{\mathrm{T}}^{\mathrm{miss}}$ suppresses the multijet background to a negligible level. Therefore it is not included as a background in the search.

7 Systematic uncertainties

The most important experimental systematic uncertainties arise from the determination of the b-tagging efficiency and mistag rate, the luminosity determination and errors associated with the calibration of the scale and resolution of the jet energy and mass. The uncertainties on the small-R jet energy scale have contributions from *in situ* calibration studies, from the dependence on pileup activity and on flavour composition of jets, and from the changes of the detector and run conditions between Run 1 and Run 2 [76, 77]. The uncertainty on the scale and resolution of large-R jet energy and mass are evaluated by comparing the ratio of calorimeter-based to track-based measurements in dijet data and simulation [78]. The b-tagging efficiency uncertainty arises mainly from the uncertainty on the measurement of the efficiency in $t\bar{t}$ events [71].

Other experimental systematic uncertainties with a smaller impact are those on the lepton energy and momentum scales, and lepton identification and trigger efficiencies [79–81]. An uncertainty on the $E_{\mathrm{T}}^{\mathrm{miss}}$ soft-term resolution and scale is taken into account [72], and uncertainties due to the lepton energy scales and resolutions, as well as reconstruction and identification efficiencies, are also considered, though they are negligible. The uncertainty on the integrated luminosity amounts to 5%, and is derived following a methodology similar to that detailed in Ref. [82],

Uncertainties are also taken into account for possible differences between data and the simulation modelling used for each process. The SHERPA W + jets and Z + jets background modelling is studied in the one and two lepton control regions, respectively, as a function of p_{T} of the vector boson, the mass m_{jj} or m_J and the azimuthal angle difference $\Delta\phi_{bb}$ between the small-R jets. The shape of the data distributions are described by the simulation with no indication that a correction is needed. A shape uncertainty on these variables is derived, encompassing the data/MC differences. An uncertainty on the SHERPA description of the flavour composition of the jets in these backgrounds is derived by comparing to MadGraph. The top background modelling is studied in the dedicated one lepton control region, and in a two lepton control region using $e\mu$ pairs. Both the p_{T} and mass of the two small-R jet system are studied. A systematic uncertainty is derived based on the data/MC comparison in these regions.

The normalisations of the $W + b\bar{b}$, $Z + b\bar{b}$, and $t\bar{t}$ contributions are determined directly from the data by leaving them as free parameters in the combined fit. The normalisations of the other W/Z + jets background contributions are obtained from theory predictions, with normalisation uncertainties assigned of 10% for $W/Z + l$, 30% for $W/Z + cl$ and a 30% uncertainty is applied to the relative normalisation of $W/Z + bc/bl/cc$ to $W/Z + b\bar{b}$. In addition, the following normalisation uncertainties are assigned to the background processes: 4% for single-top in the $s-$ and $t-$ channels, 7% for single-top in the $Wt-$ channel [83, 84], and 50% for associated $(W/Z)h$ [75, 85] production. The sources of uncertainty considered on the cross sections for the diboson production (WW, WZ and ZZ) are the renormalisation

and factorisation scales, the choice of PDFs of parton-shower and hadronisation model. The multijet contribution is estimated from data and is assigned a 50% uncertainty. Uncertainties arising from the statistical size of the simulated event sample are also taken into account.

Uncertainties on the signal acceptance from the choice of PDFs, from the choice of factorisation and renormalisation scales, and from the choice of parton-shower and underying event tune have been taken into account in the analysis. These are typically < 10% each, although they can be larger for regions with low acceptance at either low or high $E_{\mathrm{T}}^{\mathrm{miss}}$ depending on the model and the choice of masses. In addition, uncertainties arising from the limited number of simulated events are taken into account.

The contribution of the various sources of uncertainty for an example production scenario is given in Table 1.

Source of uncertainty	Impact (%)
Total	23.0
Statistical	20.5
Systematic	10.3
Experimental Uncertainties	
b-tagging	6.6
Luminosity	4.4
Jets+E_T^{miss}	2.8
Leptons	0.4
Theoretical and Modeling Uncertainties	
Top	5.1
Z+jets	3.4
Signal	2.6
W+jets	1.5
Diboson	0.6
Multijet	0.5
Vh (h$\rightarrow b\bar{b}$)	0.4

Table 1: The percentage impact of the various sources of uncertainty on the expected production cross section for signal expectation using the vector mediator model with $m_{Z'} = 2000$ GeV and $m_{\chi} = 1$ GeV, normalised with a cross section of 0.1 pb.

8 Results

Results are extracted by means of a profile likelihood fit to the reconstructed invariant mass distribution of the dijet or single large-R jet system simultaneously in all signal and control regions. The spectra entering the fit are those from the three selections associated with the number of leptons with each of these regions divided into three categories based on the number of b-tags and four kinematic regions. In the zero lepton region, this division is based on $E_{\mathrm{T}}^{\mathrm{miss}}$ while in the one and two lepton regions, it is based on $p_T(\mu, E_{\mathrm{T}}^{\mathrm{miss}})$ and $p_T(\ell, \ell)$, respectively. The shape information is not used in the zero b-tag distributions in order to simplify the fit. This division is designed to isolate, and more effectively constrain, different backgrounds. In particular, the Z + jets background is constrained both by the sample of events containing two leptons and those containing zero leptons and zero b-tags. In addition, the set of events containing one lepton

and zero b-tags constrains the W + jets background while those containing one and two b-tags constrain both the W + jets and $t\bar{t}$ backgrounds. The parameter of interest in the fit is the signal yield, while all parameters describing the systematic uncertainties and their correlations are included in the likelihood function as nuisance parameters, with Gaussian constraints, implemented using the framework described in Refs. [86, 87]. The nuisance parameters with the largest effect on the determination of the parameter of interest are the flavour-tagging and jet systematic uncertainties, together with the normalisation of the $t\bar{t}$ and $W + b\bar{b}$ backgrounds. The reconstructed Higgs boson candidate mass distribution is shown in Fig. 2 in each of the $E_{\mathrm{T}}^{\mathrm{miss}}$ categories for the set of events with two b-tags with the integrated event yields shown in Table 2. Furthermore, shown in Fig. 3 is the $E_{\mathrm{T}}^{\mathrm{miss}}$ distribution in the signal region, noting that in the two portions of the spectrum, below and above $E_{\mathrm{T}}^{\mathrm{miss}}$= 500 GeV, the requirements on the hadronic activity is taken from the small-R and large-R jets, respectively. No significant excess of events is observed above the background with the global significance of the deviation of the data from the background only prediction being 0.056.

$E_{\mathrm{T}}^{\mathrm{miss}}$ (GeV)	Resolved			Merged
	150–200	200–350	350–500	>500
$Z + jets$	259 ± 27	171 ± 13	14.6 ± 1.2	3.80 ± 0.44
$W + jets$	95 ± 28	70 ± 22	7.5 ± 2.4	2.48 ± 0.71
$t\bar{t}$ & Single top	1444 ± 44	656 ± 25	30.8 ± 1.4	4.83 ± 0.88
Multijet	21 ± 10	11 ± 5	0.58 ± 0.27	–
Diboson	17.8 ± 1.6	18.7± 1.0	2.53 ± 0.22	1.20 ± 0.12
$SMVh$	2.8 ± 1.3	2.8 ± 1.4	0.46 ± 0.23	0.15 ± 0.08
Tot. Bkg.	1840 ± 33	930 ± 20	56.5 ± 2.1	12.5 ± 1.3
Data	1830	942	56	20
Exp. Signal	80 ± 8	245 ± 18	161 ± 12	149 ± 34

Table 2: The numbers of predicted background events following the profile likelihood fit for each background process, the sum of all background components, and observed data in the 2 b-tag signal region of the resolved and merged channels for each $E_{\mathrm{T}}^{\mathrm{miss}}$ region. Statistical and systematic uncertainties are combined. The uncertainties on the total background take into account the correlation of systematic uncertainties among different background processes. An example signal expectation using the vector mediator model with $m_{Z'}$ = 2000 GeV and m_{χ} = 1 GeV, normalised with a cross section of 1 pb is also listed.

Upper limits on the production cross section for the process times branching ratio of the Higgs boson decaying to two bottom quarks ($pp \to h\chi\chi Br(h \to b\bar{b})$), set at 95% confidence level using the CL_s modified frequentist formalism [88] with the profile likelihood ratio test statistic [89], are interpreted as lower limits on the mass parameters of interest in the specific model. In Fig. 4(a) the Z'-2HDM exclusion contour in the $(m_{Z'}, m_A)$ plane for $\tan\beta = 1$, $m_{\chi} = 100$ GeV is presented, with limits more stringent than obtained in Run 1, excluding Z' masses below 1400 GeV and A masses below 500 GeV for large Z' masses. In Fig. 4(b), the exclusion contour is shown in the $(m_{Z'}, m_{\chi})$ plane for the vector mediator model described in Section 3. This interpretation was not performed in Run 1 and the mass reach for this choice of couplings excludes Z' masses below 900 GeV for low DM mass. The sharp triangular shape of the limit contours is partially a result of the pattern of the generated signal grid, indicated with blue stars in Fig. 4(a) and 4(b). Inclusion of a denser grid of signal points will alleviate this issue.

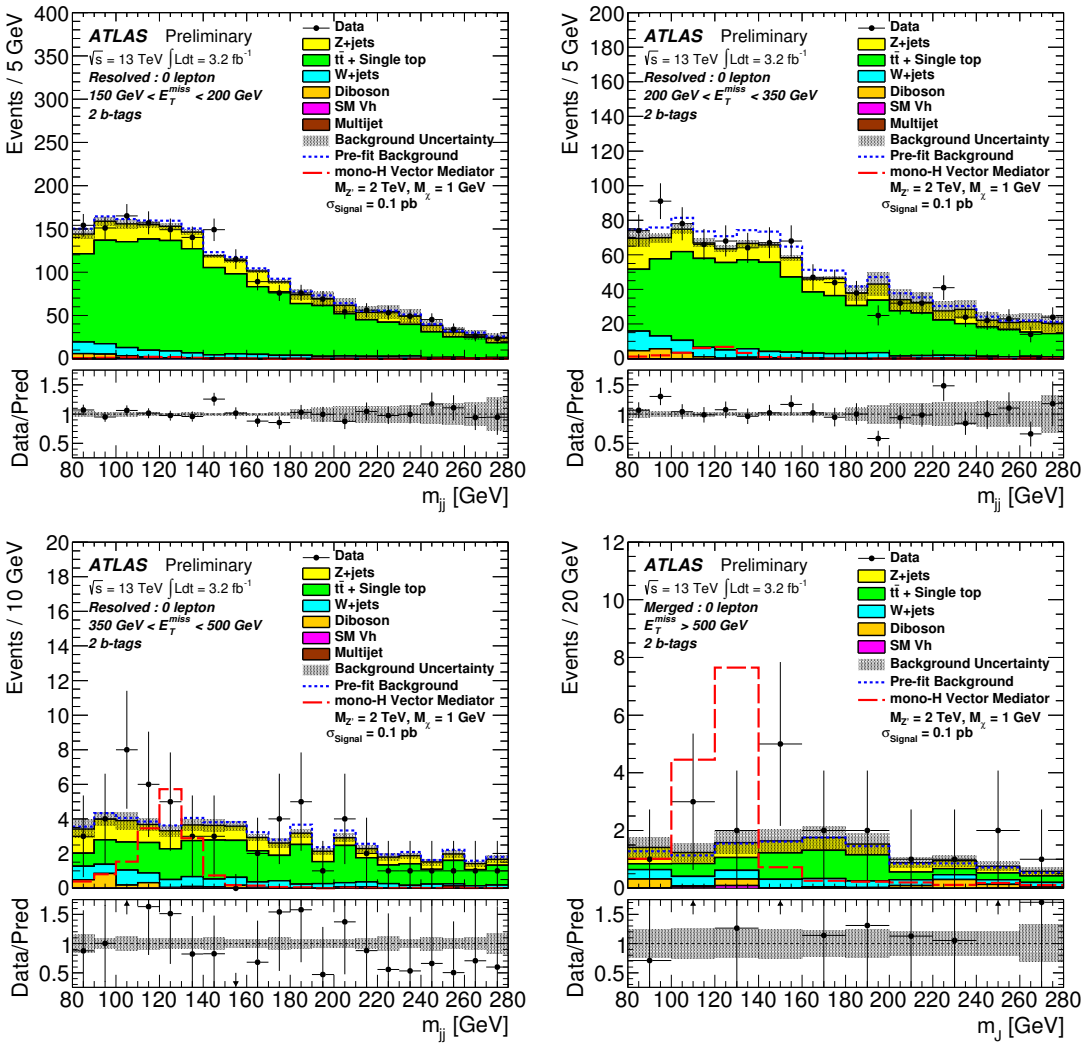

Figure 2: The reconstructed dijet and single jet invariant mass distribution in the resolved and the merged signal regions for the case where two b-tags have been identified for the four kinematic regions. The Standard Model background expectation is shown before (after) the profile likelihood fit by the dashed blue line (solid histograms) with the bottom panel showing the ratio of the data to the predicted background after the combined fit. For visual clarity the various components of the $W/Z+$jets ($b\bar{b}$, bc, bl, $c\bar{c}$, cl, ll) backgrounds have been merged and labelled $W+$jets and $Z+$jets. An example signal expectation using the vector mediator model with $m_{Z'} = 2$ TeV and $m_{\chi} = 1$ GeV, normalised with a cross section of 0.1 pb is also shown.

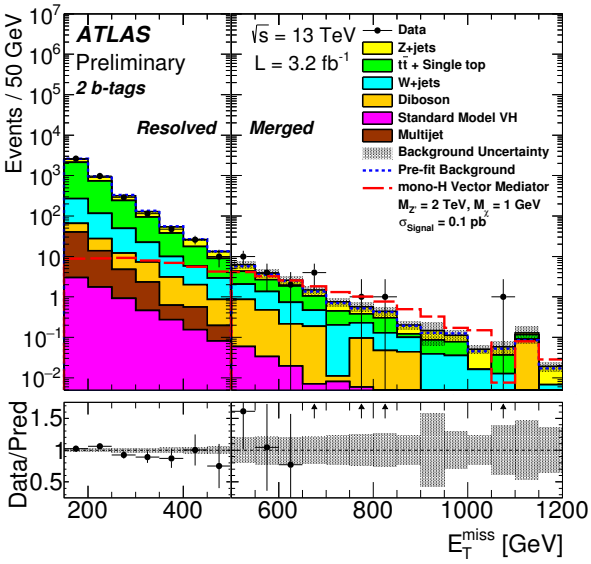

Figure 3: The reconstructed $E_{\mathrm{T}}^{\mathrm{miss}}$ distribution in the combined resolved and merged two b-tag signal regions. The Standard Model expectation is shown before (after) the profile likelihood fit by the dashed blue line (solid histograms) with the bottom panel showing the ratio of the data to the predicted background after the combined fit. For visual clarity the various components of the W/Z + jets (bb, bc, bl, cc, cl, ll) backgrounds have been merged and labelled W + jets and Z + jets. It is noted, that the multijet background was found to be negligible in the merged region. An example signal expectation using the vector mediator model with $m_{Z'} = 2$ TeV and $m_{\chi} = 1$ GeV, normalised with a cross section of 0.1 pb is also shown.

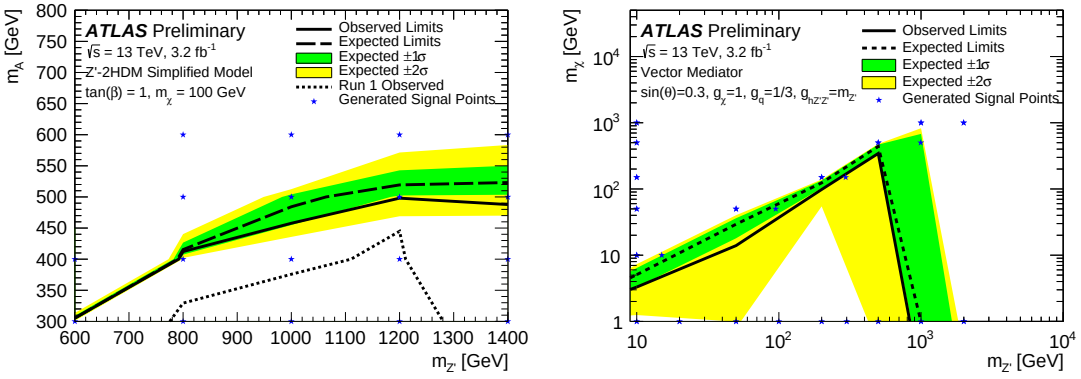

(a) (b)

Figure 4: Exclusion contours for (a) the Z'-2HDM exclusion contour in the $(m_{Z'}, m_A)$ plane for $\tan\beta = 1$, $m_{\chi} = 100$ GeV and (b) the vector mediator model in the $(m_{Z'}, m_{\chi})$ plane for $\sin\theta = 0.3$, $g_{\chi} = 1$, $g_q = 1/3$ and $g_Z = m_{Z'}$. The expected limit is given by the dashed line, while the orange and yellow bands indicate its $\pm 1\sigma$ and $\pm 2\sigma$ uncertainty bands, respectively. The observed limit is given by the solid line. In both cases, the parameter space below the limit contours are excluded at 95% CL. The sharp triangular shape of the limit contours is partially a result of the pattern of the generated signal grid, indicated with blue stars, and is discussed in Section 8.

9 Conclusion

A search is presented for dark matter pair production in association with a Higgs boson decaying into two b-quarks, using 3.2 fb^{-1} of pp collisions collected at $\sqrt{s}$ = 13 TeV by the ATLAS detector at the LHC. Two regions are considered, a low $E_{\mathrm{T}}^{\mathrm{miss}}$ region where the two b-quark jets from the Higgs boson decay are reconstructed separately and a high $E_{\mathrm{T}}^{\mathrm{miss}}$ region where they are reconstructed inside a single large-radius jet using small radius track jets.

The data are found to be consistent with the background expectation and the results are interpreted for two simplified models involving a massive vector mediator. In the Z'-two-Higgs-doublet model, constraints are placed on the $(m_{Z'}, m_A)$ space and found to exclude masses of the pseudoscalar heavy Higgs boson of up to 500 GeV for a wide range of Z' masses. In the context of the vector mediator model, constraints are placed in the two dimensional space of $(m_{Z'}, m_\chi)$ and found to exclude masses of the vector mediator of up to 900 GeV.

References

[1] G. Bertone, D. Hooper and J. Silk, *Particle dark matter: Evidence, candidates and constraints*, Phys. Rept. **405** (2005) 279, arXiv: hep-ph/0404175 [hep-ph].

[2] G. Steigman and M. S. Turner, *Cosmological constraints on the properties of weakly interacting massive particles*, Nucl. Phys. **B253** (1985) 375.

[3] D. Bauer et al., *Dark matter in the coming decade: Complementary paths to discovery and beyond*, Phys. Dark Univ. **7-8** (2015) 16, arXiv: 1305.1605 [hep-ph].

[4] L. Evans and P. Bryant, *LHC Machine*, JINST **3** (2008) S08001.

[5] ATLAS Collaboration, *Search for new phenomena in final states with an energetic jet and large missing transverse momentum in pp collisions at* $\sqrt{s} = 8$ *TeV with the ATLAS detector*, Eur. Phys. J. **C75** (2015) 299, arXiv: 1502.01518 [hep-ex].

[6] CMS Collaboration, *Search for dark matter, extra dimensions, and unparticles in monojet events in proton–proton collisions at* $\sqrt{s} = 8$ *TeV*, Eur. Phys. J. **C75** (2015) 235, arXiv: 1408.3583 [hep-ex].

[7] ATLAS Collaboration, *Search for dark matter in events with heavy quarks and missing transverse momentum in pp collisions with the ATLAS detector*, Eur. Phys. J. **C75** (2015) 92, arXiv: 1410.4031 [hep-ex].

[8] CMS Collaboration, *Search for Monotop Signatures in Proton-Proton Collisions at* $\sqrt{s} = 8$ *TeV*, Phys. Rev. Lett. **114** (2015) 101801, arXiv: 1410.1149 [hep-ex].

[9] CMS Collaboration, *Search for the production of dark matter in association with top-quark pairs in the single-lepton final state in proton-proton collisions at sqrt(s) = 8 TeV*, JHEP **06** (2015) 121, arXiv: 1504.03198 [hep-ex].

[10] ATLAS Collaboration, *Search for new phenomena in events with a photon and missing transverse momentum in pp collisions at* $\sqrt{s} = 8$ *TeV with the ATLAS detector*, Phys. Rev. **D91** (2015) 012008, arXiv: 1411.1559 [hep-ex].

[11] CMS Collaboration, *Search for Dark Matter and Large Extra Dimensions in pp Collisions Yielding a Photon and Missing Transverse Energy*, Phys. Rev. Lett. **108** (2012) 261803, arXiv: 1204.0821 [hep-ex].

[12] CMS Collaboration, *Search for new phenomena in monophoton final states in proton-proton collisions at* $\sqrt{s} = 8$ *TeV*, Phys. Lett. **B755** (2016) 102, arXiv: 1410.8812 [hep-ex].

[13] CMS Collaboration, *Search for physics beyond the standard model in final states with a lepton and missing transverse energy in proton-proton collisions at sqrt(s) = 8 TeV*, Phys. Rev. **D91** (2015) 092005, arXiv: 1408.2745 [hep-ex].

[14] ATLAS Collaboration, *Search for new particles in events with one lepton and missing transverse momentum in pp collisions at* $\sqrt{s} = 8$ *TeV with the ATLAS detector*, JHEP **09** (2014) 037, arXiv: 1407.7494 [hep-ex].

[15] ATLAS Collaboration, *Search for dark matter in events with a Z boson and missing transverse momentum in pp collisions at* $\sqrt{s}$*=8 TeV with the ATLAS detector*, Phys. Rev. **D90** (2014) 012004, arXiv: 1404.0051 [hep-ex].

[16] ATLAS Collaboration, *Search for dark matter in events with a hadronically decaying W or Z boson and missing transverse momentum in pp collisions at $\sqrt{s}$=8 TeV with the ATLAS detector*, Phys. Rev. Lett. **112** (2014) 041802, arXiv: 1309.4017 [hep-ex].

[17] CMS Collaboration, *Search for dark matter and unparticles produced in association with a Z boson in proton-proton collisions at sqrt(s) = 8 TeV*, (2015), arXiv: 1511.09375 [hep-ex].

[18] ATLAS Collaboration, *Observation of a new particle in the search for the Standard Model Higgs boson with the ATLAS detector at the LHC*, Phys. Lett. **B716** (2012) 1, arXiv: 1207.7214 [hep-ex].

[19] CMS Collaboration, *Observation of a new boson at a mass of 125 GeV with the CMS experiment at the LHC*, Phys. Lett. **B716** (2012) 30, arXiv: 1207.7235 [hep-ex].

[20] L. Carpenter et al., *Mono-Higgs-boson: A new collider probe of dark matter*, Phys. Rev. **D89** (2014) 075017, arXiv: 1312.2592 [hep-ph].

[21] A. Berlin, T. Lin and L.-T. Wang, *Mono-Higgs detection of dark matter at the LHC*, JHEP **06** (2014) 078, arXiv: 1402.7074 [hep-ph].

[22] ATLAS Collaboration, *Search for Dark Matter in Events with Missing Transverse Momentum and a Higgs Boson Decaying to Two Photons in pp Collisions at $\sqrt{s}$ = 8 TeV with the ATLAS Detector*, Phys. Rev. Lett. **115** (2015) 131801, arXiv: 1506.01081 [hep-ex].

[23] ATLAS Collaboration, *Search for dark matter produced in association with a Higgs boson decaying to two bottom quarks in pp collisions at $\sqrt{s}$ = 8 TeV with the ATLAS detector*, (2015), arXiv: 1510.06218 [hep-ex].

[24] J. Abdallah et al., *Simplified Models for Dark Matter Searches at the LHC*, Phys. Dark Univ. **9-10** (2015) 8, arXiv: 1506.03116 [hep-ph].

[25] D. Abercrombie et al., *Dark Matter Benchmark Models for Early LHC Run-2 Searches: Report of the ATLAS/CMS Dark Matter Forum*, (2015), arXiv: 1507.00966 [hep-ex].

[26] F. del Aguila et al., *Superstring Inspired Models*, Nucl. Phys. **B272** (1986) 413.

[27] G. C. Branco et al., *Theory and phenomenology of two-Higgs-doublet models*, Phys. Rept. **516** (2012) 1, arXiv: 1106.0034 [hep-ph].

[28] J. Beringer et al., *Review of particle physics (RPP), Section* 10.7, Phys. Rev. **D86** (2012) 010001.

[29] CDF Collaboration, *Search for new particles decaying into dijets in proton-antiproton collisions at $\sqrt{s}$ = 1.96 TeV*, Phys. Rev. **D79** (2009) 112002, arXiv: 0812.4036 [hep-ex].

[30] CMS Collaboration, *Search for narrow resonances and quantum black holes in inclusive and b-tagged dijet mass spectra from pp collisions at $\sqrt{s}$ = 7 TeV*, JHEP **01** (2013) 013, arXiv: 1210.2387 [hep-ex].

[31] CMS Collaboration, *Search for resonances and quantum black holes using dijet mass spectra in proton-proton collisions at $\sqrt{s}$ = 8 TeV*, Phys. Rev. **D91** (2015) 052009, arXiv: 1501.04198 [hep-ex].

[32] ATLAS Collaboration, *The ATLAS Experiment at the CERN Large Hadron Collider*, JINST **3** (2008) S08003.

[33] ATLAS Collaboration, *ATLAS Insertable B-Layer Technical Design Report*, (2010), URL: https://cds.cern.ch/record/1291633.

[34] ATLAS Collaboration, *Expected performance of the ATLAS b-tagging algorithms in Run-2*, (2015), URL: https://cds.cern.ch/record/2037697.

[35] ATLAS Collaboration, *Commissioning of the ATLAS b-tagging algorithms using $t\bar{t}$ events in early Run-2 data*, (2015), URL: https://cds.cern.ch/record/2047871.

[36] J. Alwall et al., *MadGraph 5 : going beyond*, JHEP **06** (2011) 128, arXiv: 1106.0522 [hep-ph].

[37] R. D. Ball et al., *Parton distributions with LHC data*, Nucl. Phys. **B867** (2013) 244, arXiv: 1207.1303 [hep-ph].

[38] ATLAS Collaboration, *ATLAS Pythia 8 tunes to 7 TeV data*, ATL-PHYS-PUB-2014-021, 2014, URL: http://cdsweb.cern.ch/record/1966419.

[39] T. Han and S. Willenbrock, *QCD correction to the p p —> W H and Z H total cross-sections*, Phys. Lett. **B273** (1991) 167.

[40] O. Brein, A. Djouadi and R. Harlander, *NNLO QCD corrections to the Higgs-strahlung processes at hadron colliders*, Phys. Lett. **B579** (2004) 149, arXiv: hep-ph/0307206 [hep-ph].

[41] M. L. Ciccolini, S. Dittmaier and M. Kramer, *Electroweak radiative corrections to associated WH and ZH production at hadron colliders*, Phys. Rev. **D68** (2003) 073003, arXiv: hep-ph/0306234 [hep-ph].

[42] T. Gleisberg et al., *Event generation with SHERPA 1.1*, JHEP **02** (2009) 007, arXiv: 0811.4622 [hep-ph].

[43] H.-L. Lai et al., *New parton distributions for collider physics*, Phys. Rev. D **82** (2010) 074024, arXiv: 1007.2241 [hep-ph].

[44] T. Gleisberg and S. Höche, *Comix, a new matrix element generator*, JHEP **12** (2008) 039, arXiv: 0808.3674 [hep-ph].

[45] F. Cascioli, P. Maierhofer and S. Pozzorini, *Scattering Amplitudes with Open Loops*, Phys. Rev. Lett. **108** (2012) 111601, arXiv: 1111.5206 [hep-ph].

[46] S. Schumann and F. Krauss, *A Parton shower algorithm based on Catani-Seymour dipole factorisation*, JHEP **03** (2008) 038, arXiv: 0709.1027 [hep-ph].

[47] S. Höche et al., *QCD matrix elements + parton showers: The NLO case*, JHEP **04** (2013) 027, arXiv: 1207.5030 [hep-ph].

[48] K. Melnikov and F. Petriello, *Electroweak gauge boson production at hadron colliders through $O(\alpha_s^2)$*, Phys. Rev. D **74** (2006) 114017, arXiv: hep-ph/0609070.

[49] S. Alioli et al., *A general framework for implementing NLO calculations in shower Monte Carlo programs: the POWHEG BOX*, JHEP **06** (2010) 043, arXiv: 1002.2581 [hep-ph].

[50] T. Sjöstrand, S. Mrenna and P. Z. Skands, *PYTHIA 6.4 Physics and Manual*, JHEP **05** (2006) 026, arXiv: hep-ph/0603175.

[51] P. M. Nadolsky et al., *Implications of CTEQ global analysis for collider observables*, Phys. Rev. **D78** (2008) 013004, arXiv: 0802.0007 [hep-ph].

[52] P. Z. Skands, *Tuning Monte Carlo generators: the Perugia tunes*, Phys. Rev. **D82** (2010) 074018, arXiv: 1005.3457 [hep-ph].

[53] M. Czakon, P. Fiedler and A. Mitov, *The total top quark pair production cross-section at hadron colliders through $O(\alpha_S^4)$*, Phys. Rev. Lett. **110** (2013) 252004, arXiv: 1303.6254 [hep-ph].

[54] N. Kidonakis, *Next-to-next-to-leading-order collinear and soft gluon corrections for t-channel single top quark production*, Phys. Rev. **D83** (2011) 091503, arXiv: 1103.2792 [hep-ph].

[55] N. Kidonakis, *NNLL resummation for s-channel single top quark production*, Phys. Rev. **D81** (2010) 054028, arXiv: 1001.5034 [hep-ph].

[56] N. Kidonakis, *Two-loop soft anomalous dimensions for single top quark associated production with a W^- or H^-*, Phys. Rev. **D82** (2010) 054018, arXiv: 1005.4451 [hep-ph].

[57] ATLAS Collaboration, *The ATLAS Simulation Infrastructure*, Eur. Phys. J. **C70** (2010) 823, arXiv: 1005.4568 [physics.ins-det].

[58] S. Agostinelli et al., *GEANT4: A Simulation toolkit*, Nucl. Instrum. Meth. **A506** (2003) 250.

[59] T. Sjöstrand, S. Mrenna and P. Z. Skands, *A brief introduction to PYTHIA 8.1*, Comput. Phys. Commun. **178** (2008) 852, arXiv: 0710.3820 [hep-ph].

[60] ATLAS Collaboration, *Summary of ATLAS Pythia 8 tunes*, (2012), URL: http://cds.cern.ch/record/1474107.

[61] G. Watt and R. Thorne, *Study of Monte Carlo approach to experimental uncertainty propagation with MSTW 2008 PDFs*, JHEP **08** (2012) 052, arXiv: 1205.4024 [hep-ph].

[62] ATLAS Collaboration, *Measurement of the muon reconstruction performance of the ATLAS detector using 2011 and 2012 LHC proton–proton collision data*, Eur. Phys. J. **C74** (2014) 3130, arXiv: 1407.3935 [hep-ex].

[63] ATLAS Collaboration, *Electron efficiency measurements with the ATLAS detector using the 2012 LHC proton-proton collision data*, ATLAS-CONF-2014-032 (2014).

[64] M. Cacciari, G. P. Salam and G. Soyez, *The Anti-k(t) jet clustering algorithm*, JHEP **04** (2008) 063, arXiv: 0802.1189 [hep-ph].

[65] M. Cacciari, G. P. Salam and G. Soyez, *The Catchment Area of Jets*, JHEP **04** (2008) 005, arXiv: 0802.1188 [hep-ph].

[66] D. Krohn, J. Thaler and L.-T. Wang, *Jet trimming*, JHEP **02** (2010) 084, arXiv: 0912.1342 [hep-ph].

[67] S. Catani et al., *Longitudinally invariant $K_\perp$ clustering algorithms for hadron hadron collisions*, Nucl. Phys. **B406** (1993) 187.

[68] ATLAS Collaboration, *Jet energy measurement with the ATLAS detector in proton-proton collisions at $\sqrt{s} = 7$ TeV*, Eur. Phys. J. **C73** (2013) 2304, arXiv: 1112.6426 [hep-ex].

[69] ATLAS Collaboration, *Tagging and suppression of pileup jets*, ATLAS-CONF-2014-018 (2014).

[70] M. Cacciari and G. P. Salam, *Pileup subtraction using jet areas*, Phys. Lett. **B659** (2008) 119, arXiv: 0707.1378 [hep-ph].

[71] ATLAS Collaboration, *Performance of b-Jet Identification in the ATLAS Experiment*, accepted by JINST (2015), arXiv: 1512.01094 [hep-ex].

[72] ATLAS Collaboration, *Expected performance of missing transverse momentum reconstruction for the ATLAS detector at $\sqrt{s}$ = 13 TeV*, (2015), URL: https://cds.cern.ch/record/2037700.

[73] ATLAS Collaboration, *Performance of Missing Transverse Momentum Reconstruction in Proton-Proton Collisions at 7 TeV with ATLAS*, Eur. Phys. J. **C72** (2012) 1844, arXiv: 1108.5602 [hep-ex].

[74] ATLAS Collaboration, *Expected Performance of Boosted Higgs($\rightarrow b\bar{b}$) Boson Identification with the ATLAS Detector at $\sqrt{s}$ = 13 TeV*, (2015), URL: https://cds.cern.ch/record/2042155.

[75] ATLAS Collaboration, *Search for the $b\bar{b}$ decay of the Standard Model Higgs boson in associated $(W/Z)H$ production with the ATLAS detector*, JHEP **01** (2015) 069, arXiv: 1409.6212 [hep-ex].

[76] ATLAS Collaboration, *Jet energy measurement and its systematic uncertainty in proton-proton collisions at $\sqrt{s}$ = 7 TeV with the ATLAS detector*, Eur. Phys. J. **C75** (2015) 17, arXiv: 1406.0076 [hep-ex].

[77] ATLAS Collaboration, *Jet Calibration and Systematic Uncertainties for Jets Reconstructed in the ATLAS Detector at $\sqrt{s}$ = 13 TeV*, (2015), URL: https://cds.cern.ch/record/2037613.

[78] ATLAS Collaboration, *Identification of boosted, hadronically-decaying W and Z bosons in $\sqrt{s}$ = 13 TeV Monte Carlo simulations for ATLAS*, (2015), URL: https://cds.cern.ch/record/2041461.

[79] ATLAS Collaboration, *Muon reconstruction performance in early $\sqrt{s}$=13 TeV data*, (2015), URL: https://cds.cern.ch/record/2047831.

[80] ATLAS Collaboration, *Electron reconstruction and identification efficiency measurements with the ATLAS detector using the 2011 LHC proton-proton collision data*, Eur. Phys. J. **C74** (2014) 2941, arXiv: 1404.2240 [hep-ex].

[81] ATLAS Collaboration, *Electron and photon energy calibration with the ATLAS detector using LHC Run 1 data*, Eur. Phys. J. **C74** (2014) 3071, arXiv: 1407.5063 [hep-ex].

[82] ATLAS Collaboration, *Improved luminosity determination in pp collisions at $\sqrt{s}$ = 7 TeV using the ATLAS detector at the LHC*, Eur. Phys. J. **C73** (2013) 2518, arXiv: 1302.4393 [hep-ex].

[83] M. Aliev et al., *HATHOR: HAdronic Top and Heavy quarks crOss section calculatoR*, Comput. Phys. Commun. **182** (2011) 1034, arXiv: 1007.1327 [hep-ph].

[84] P. Kant et al., *HatHor for single top-quark production: Updated predictions and uncertainty estimates for single top-quark production in hadronic collisions*, Comput. Phys. Commun. **191** (2015) 74, arXiv: 1406.4403 [hep-ph].

[85] CMS Collaboration, *Search for the standard model Higgs boson produced in association with a W or a Z boson and decaying to bottom quarks*, Phys. Rev. **D89** (2014) 012003, arXiv: 1310.3687 [hep-ex].

[86] W. Verkerke and D. P. Kirkby, *The RooFit toolkit for data modeling*, eConf **C0303241** (2003), arXiv: physics/0306116 [physics].

[87] L. Moneta et al., *The RooStats Project*, PoS **ACAT2010** (2010) 057, arXiv: 1009.1003 [physics.data-an].

[88] A. L. Read, *Presentation of search results: the CL_s technique*, Journal of Physics G: Nuclear and Particle Physics **28** (2002) 2693, URL: http://stacks.iop.org/0954-3899/28/i=10/a=313.

[89] G. Cowan et al., *Asymptotic formulae for likelihood-based tests of new physics*, Eur. Phys. J. **C71** (2011) 1554, [Erratum: Eur. Phys. J.C73,2013(2501)], arXiv: 1007.1727 [physics.data-an].

Auxiliary material

Region	Signal Region	Z+jets Control Region	W+jets and $t\bar{t}$ Control Region
Trigger	$E_{\mathrm{T}}^{\mathrm{miss}}$	$E_{\mathrm{T}}^{\mathrm{miss}}$	Single Lepton
N(lepton)	0 μ and e	Exactly 1 μ	Exactly 2 μ or e
Merged	$E_{\mathrm{T}}^{\mathrm{miss}}$ >500 GeV	$p_T(\mu, E_{\mathrm{T}}^{\mathrm{miss}})$>500 GeV	$p_T(\ell, \ell)$>500 GeV
	$p_{\mathrm{T}}^{\mathrm{miss}}$>30 GeV	$p_T(\mu, p_{\mathrm{T}}^{\mathrm{miss}})$>30 GeV	–
	N(large-R jets)≥1		
	Division by track jet b-tags		
	Final discriminant = Large-R jet mass		
Resolved	$E_{\mathrm{T}}^{\mathrm{miss}}$ =[150,500] GeV	$p_T(\mu, E_{\mathrm{T}}^{\mathrm{miss}})$=[150,500] GeV	$p_T(\ell, \ell)$=[150,500] GeV
	$p_{\mathrm{T}}^{\mathrm{miss}}$>30 GeV	$p_T(\mu, p_{\mathrm{T}}^{\mathrm{miss}})$>30 GeV	–
	$\min\left(\Delta\phi\left(\vec{E}_{\mathrm{T}}^{\mathrm{miss}}, \mathrm{jets}\right)\right) > 20°$		–
	$\Delta\phi\left(\vec{E}_{\mathrm{T}}^{\mathrm{miss}}, \vec{p}_{\mathrm{T}}^{\mathrm{miss}}\right)$		–
	N(central small-R jets)≥2		
	$p_T(j_{h_{\mathrm{r}}}^1)$ ≥45 GeV or $p_T(j_{h_{\mathrm{r}}}^2)$ ≥45 GeV		
	$\Delta\phi\left(j_{h_{\mathrm{r}}}^1, j_{h_{\mathrm{r}}}^2\right) < 140°$		
	H_T(2jets)>120 GeV or H_T(3jets)>150 GeV		
	$\Delta\phi\left(\vec{E}_{\mathrm{T}}^{\mathrm{miss}}, h_{\mathrm{r}}\right) > 120°$		
	–	–	$E_{\mathrm{T}}^{\mathrm{miss}}/\,\Sigma p_T$(jets, leptons) < 3.5
	Division by small-R calorimeter jet b-tags		
	Final discriminant = Dijet mass		

Table 3: A summary of the main analysis selection criteria. Refer to the main body for detailed descriptions of the selection criteria.

Model	Observed	Expected	Expected +1σ	Expected -1σ
Z'-2HDM : $m_{Z'}$=1000 GeV m_A=300 GeV	0.24	0.18	0.25	0.13
Z'-2HDM : $m_{Z'}$=1000 GeV m_A=400 GeV	0.447	0.338	0.471	0.244
Z'-2HDM : $m_{Z'}$=1000 GeV m_A=500 GeV	2.707	2.017	2.807	1.453
Z'-2HDM : $m_{Z'}$=1000 GeV m_A=600 GeV	15.993	11.976	16.668	8.63
Z'-2HDM : $m_{Z'}$=1000 GeV m_A=700 GeV	73.447	55.625	77.416	40.08
Z'-2HDM : $m_{Z'}$=1000 GeV m_A=800 GeV	232.859	175.581	244.344	126.52
Z'-2HDM : $m_{Z'}$=1200 GeV m_A=300 GeV	0.391	0.237	0.33	0.171
Z'-2HDM : $m_{Z'}$=1200 GeV m_A=400 GeV	0.617	0.382	0.532	0.276
Z'-2HDM : $m_{Z'}$=1200 GeV m_A=500 GeV	1.774	1.189	1.655	0.857
Z'-2HDM : $m_{Z'}$=1200 GeV m_A=600 GeV	5.781	4.094	5.699	2.95
Z'-2HDM : $m_{Z'}$=1200 GeV m_A=700 GeV	23.84	16.754	23.314	12.069
Z'-2HDM : $m_{Z'}$=1200 GeV m_A=800 GeV	89.123	60.645	84.387	43.687
Z'-2HDM : $m_{Z'}$=1400 GeV m_A=300 GeV	0.458	0.291	0.406	0.21
Z'-2HDM : $m_{Z'}$=1400 GeV m_A=400 GeV	0.647	0.398	0.554	0.287
Z'-2HDM : $m_{Z'}$=1400 GeV m_A=500 GeV	1.905	1.17	1.629	0.844
Z'-2HDM : $m_{Z'}$=1400 GeV m_A=600 GeV	6.242	3.681	5.12	2.652
Z'-2HDM : $m_{Z'}$=1400 GeV m_A=700 GeV	18.477	11.251	15.665	8.111
Z'-2HDM : $m_{Z'}$=1400 GeV m_A=800 GeV	54.238	33.654	46.832	24.244
Z'-2HDM : $m_{Z'}$=600 GeV m_A=300 GeV	0.708	0.777	1.081	0.56
Z'-2HDM : $m_{Z'}$=600 GeV m_A=400 GeV	20.52	19.009	26.455	13.697
Z'-2HDM : $m_{Z'}$=800 GeV m_A=300 GeV	0.431	0.347	0.483	0.25
Z'-2HDM : $m_{Z'}$=800 GeV m_A=400 GeV	0.957	0.814	1.133	0.587
Z'-2HDM : $m_{Z'}$=800 GeV m_A=500 GeV	7.451	6.891	9.59	4.965
Z'-2HDM : $m_{Z'}$=800 GeV m_A=600 GeV	80.99	70.401	97.977	50.726
Vector Med. : $m_{Z'}$=1000 GeV m_χ=1000 GeV	59793.935	35127.282	48898.236	25309.802
Vector Med. : $m_{Z'}$=1000 GeV m_χ=1 GeV	1.598	1.009	1.405	0.727
Vector Med. : $m_{Z'}$=100 GeV m_χ=1 GeV	0.677	0.486	0.676	0.35
Vector Med. : $m_{Z'}$=10 GeV m_χ=1000 GeV	1079043933.25	635549735.676	884733339.906	458152056.646
Vector Med. : $m_{Z'}$=10 GeV m_χ=10 GeV	106.265	73.903	102.851	53.251
Vector Med. : $m_{Z'}$=10 GeV m_χ=150 GeV	67999.319	44214.589	61535.834	31860.089
Vector Med. : $m_{Z'}$=10 GeV m_χ=1 GeV	0.713	0.52	0.723	0.374
Vector Med. : $m_{Z'}$=10 GeV m_χ=500 GeV	11296526.02	6702983.881	9327865.103	4829690.622
Vector Med. : $m_{Z'}$=10 GeV m_χ=50 GeV	3415.33	2481.898	3454.074	1788.35
Vector Med. : $m_{Z'}$=15 GeV m_χ=10 GeV	24.909	20.905	29.094	15.063
Vector Med. : $m_{Z'}$=1995 GeV m_χ=1000 GeV	210.534	119.527	166.345	86.136
Vector Med. : $m_{Z'}$=2000 GeV m_χ=1 GeV	8.121	4.686	6.522	3.376
Vector Med. : $m_{Z'}$=200 GeV m_χ=150 GeV	87.717	54.459	75.792	39.24
Vector Med. : $m_{Z'}$=200 GeV m_χ=1 GeV	0.655	0.472	0.657	0.34
Vector Med. : $m_{Z'}$=20 GeV m_χ=1 GeV	0.595	0.495	0.689	0.357
Vector Med. : $m_{Z'}$=295 GeV m_χ=150 GeV	3.794	2.662	3.705	1.918
Vector Med. : $m_{Z'}$=300 GeV m_χ=1 GeV	0.673	0.489	0.68	0.352
Vector Med. : $m_{Z'}$=500 GeV m_χ=1 GeV	0.793	0.597	0.832	0.431
Vector Med. : $m_{Z'}$=500 GeV m_χ=500 GeV	2834.237	1649.074	2294.667	1188.15
Vector Med. : $m_{Z'}$=50 GeV m_χ=1 GeV	0.817	0.54	0.752	0.389
Vector Med. : $m_{Z'}$=50 GeV m_χ=50 GeV	134.311	88.443	123.088	63.729
Vector Med. : $m_{Z'}$=95 GeV m_χ=50 GeV	5.442	4.06	5.65	2.925
Vector Med. : $m_{Z'}$=995 GeV m_χ=500 GeV	18.613	11.68	16.254	8.416

Table 4: A compilation of the numerical results on the limits on the signal strength for the specific model parameters used. For the Z'-2HDM model, these parameters are $\tan\beta = 1.0$ and $g_Z = 0.8$ and for the vector mediator model, these parameters are $g_\chi = 1.0$, $g_\mathrm{q} = 1/3$, $g_{Z'} = m_{Z'}$, $\sin\theta = 0.3$.

Model	Observed [pb]	Expected [pb]	Expected +1σ [pb]	Expected +1σ [pb]
EFT Dimension 4 : m_χ=1000 GeV	0.028	0.017	0.024	0.013
EFT Dimension 4 : m_χ=500 GeV	0.032	0.02	0.028	0.014
EFT Dimension 4 : m_χ=100 GeV	0.078	0.044	0.061	0.032
EFT Dimension 4 : m_χ=65 GeV	0.11	0.063	0.088	0.046
EFT Dimension 5 : m_χ=1000 GeV	0.029	0.018	0.026	0.013
EFT Dimension 5 : m_χ=500 GeV	0.035	0.021	0.029	0.015
EFT Dimension 5 : m_χ=100 GeV	0.074	0.043	0.06	0.031
EFT Dimension 5 : m_χ=65 GeV	0.104	0.061	0.086	0.044
EFT Dimension 6 : m_χ=1000 GeV	0.03	0.019	0.026	0.013
EFT Dimension 6 : m_χ=500 GeV	0.033	0.02	0.028	0.015
EFT Dimension 6 : m_χ=100 GeV	0.068	0.04	0.055	0.029
EFT Dimension 6 : m_χ=65 GeV	0.086	0.05	0.069	0.036
EFT Dimension 7 : m_χ=1000 GeV	0.024	0.016	0.023	0.012
EFT Dimension 7 : m_χ=500 GeV	0.025	0.017	0.023	0.012
EFT Dimension 7 : m_χ=100 GeV	0.028	0.018	0.025	0.013
EFT Dimension 7 : m_χ=1 GeV	0.028	0.018	0.025	0.013

Table 5: A compilation of the numerical results on cross section limits of the effective field theory models.

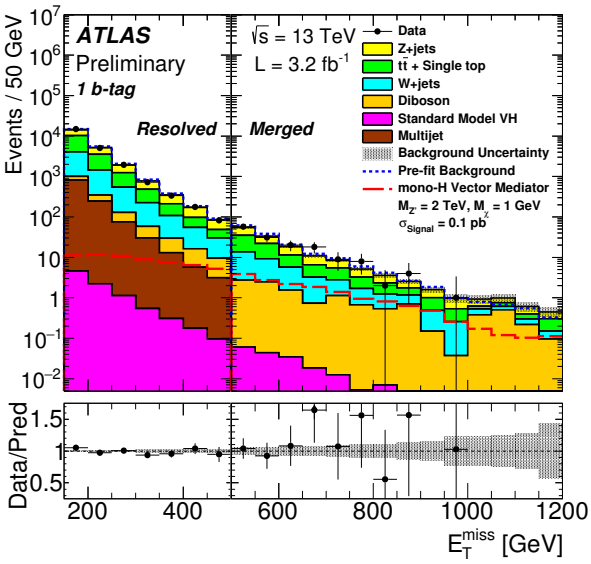

(a)

Figure 5: The reconstructed $E_{\mathrm{T}}^{\mathrm{miss}}$ distribution in the 1 b-tag 0 lepton selection region.

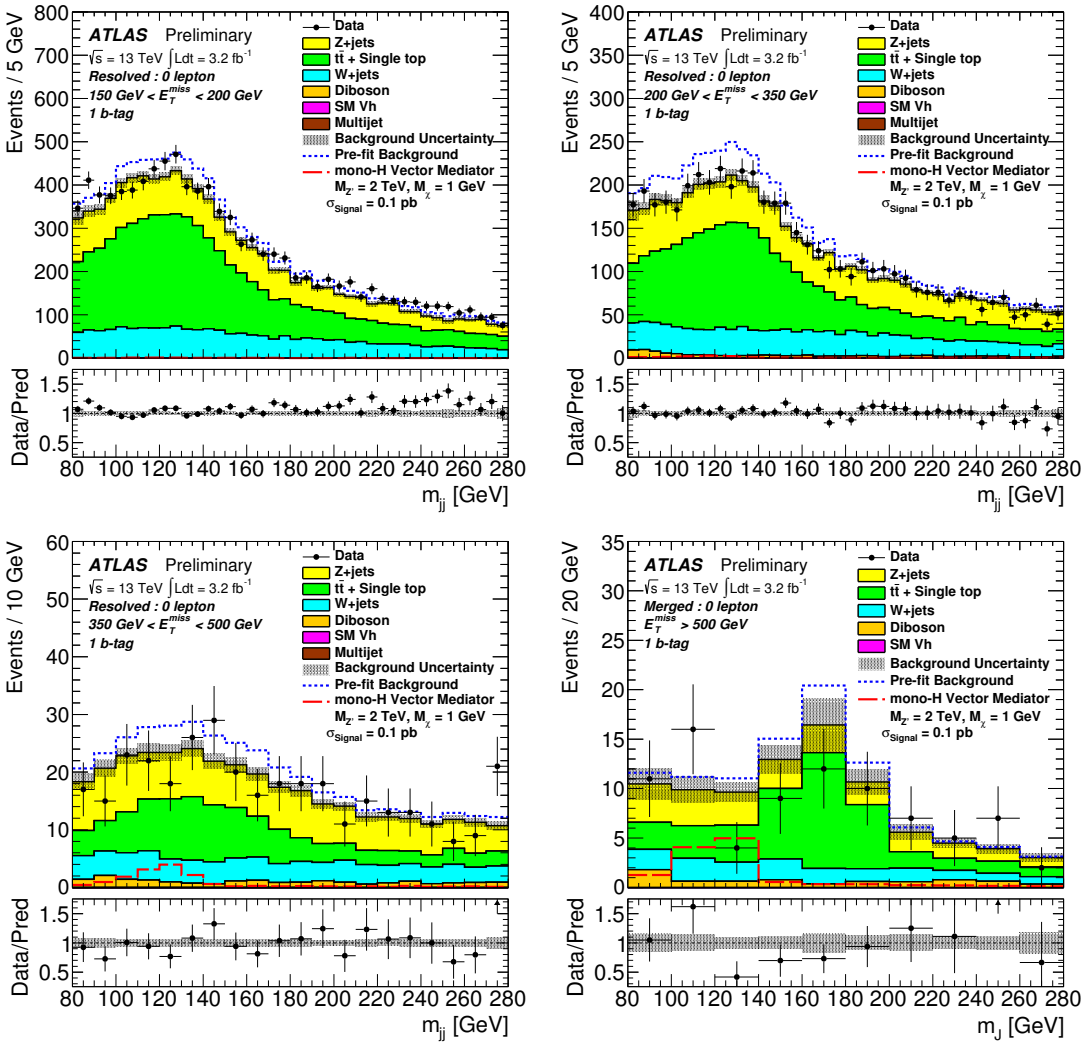

Figure 6: Post-fit plots of the invariant mass of the two signal jets for the 0 lepton control region for 1 tag events.

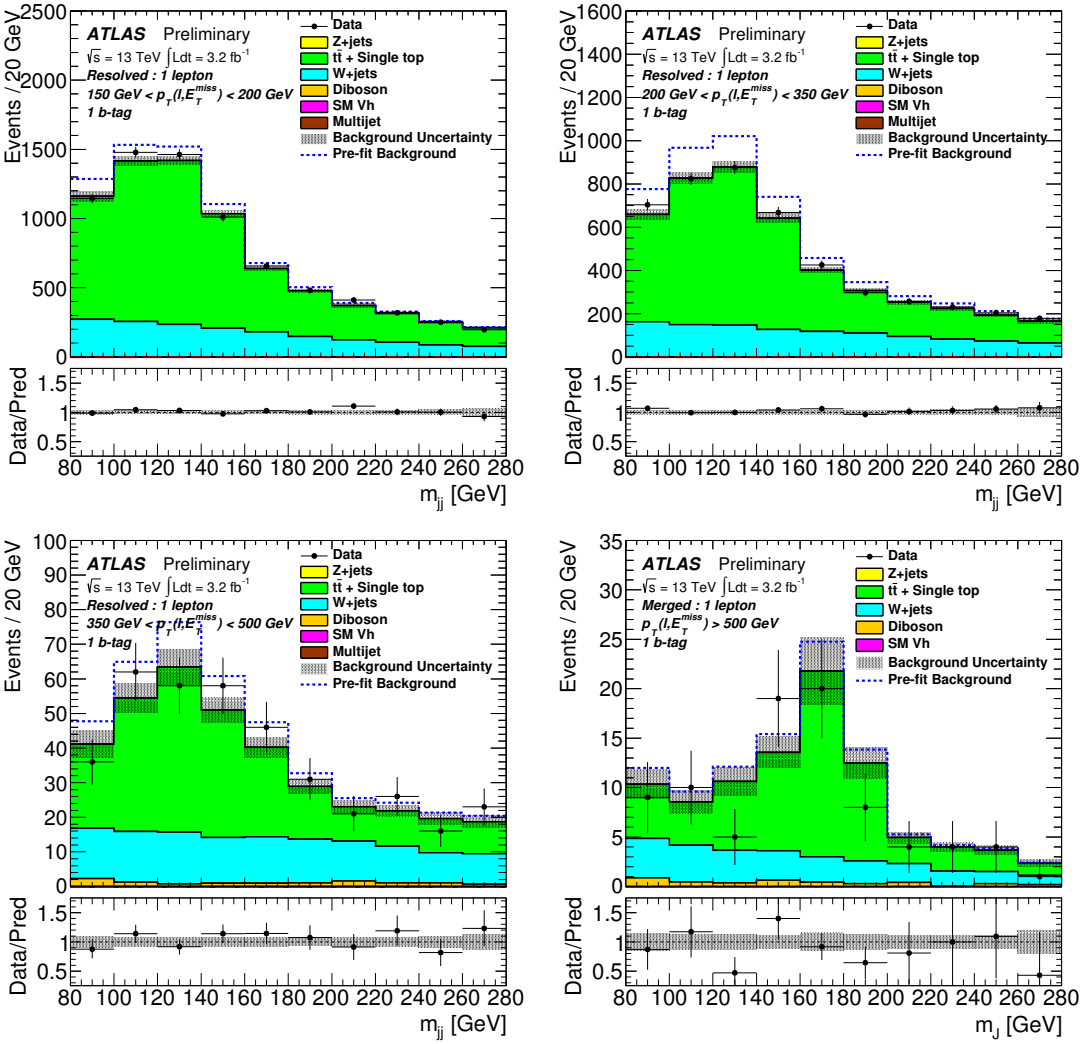

Figure 7: Post-fit plots of the invariant mass of the two signal jets for the 1 lepton control region for 1 tag events.

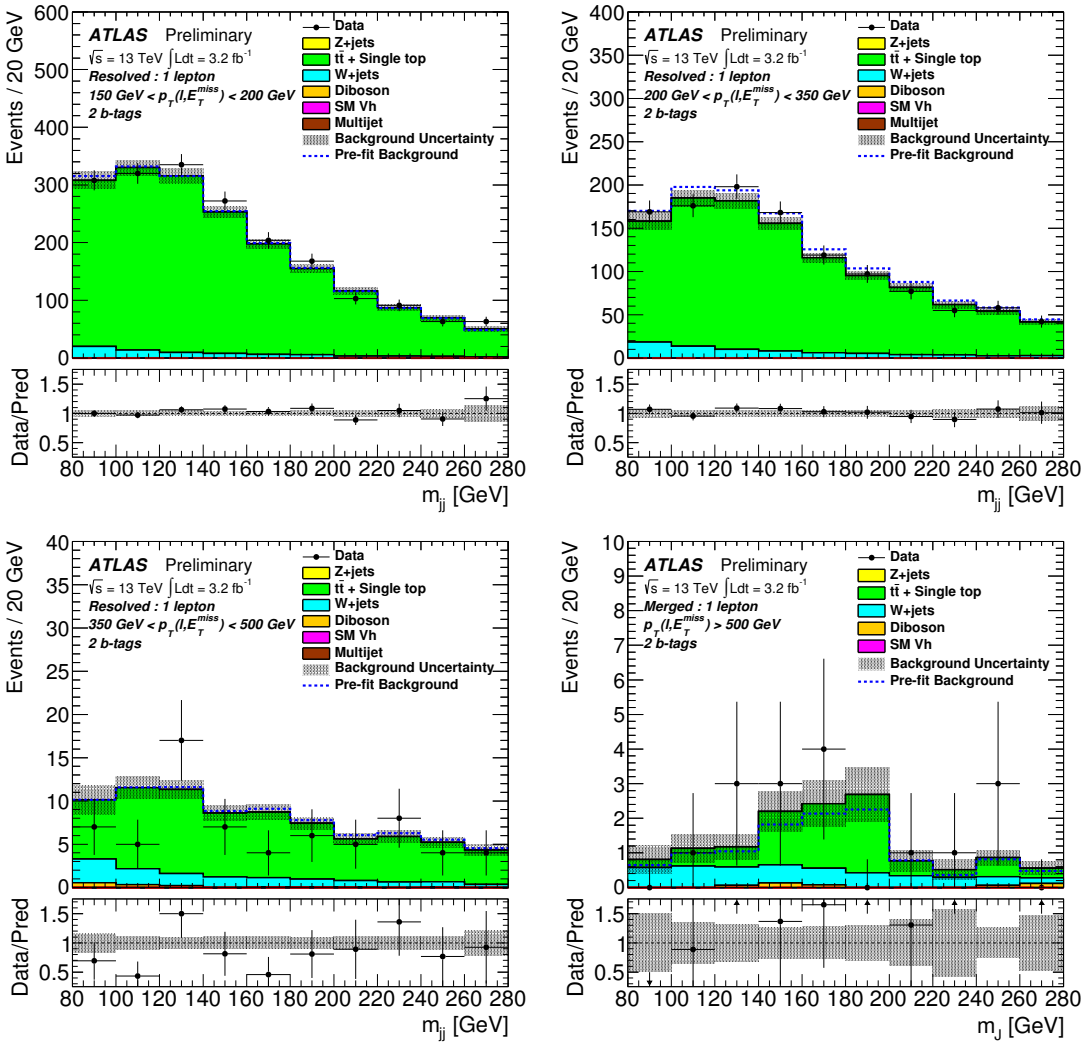

Figure 8: Post-fit plots of the invariant mass of the two signal jets for the 1 lepton control region for 2 tag events.

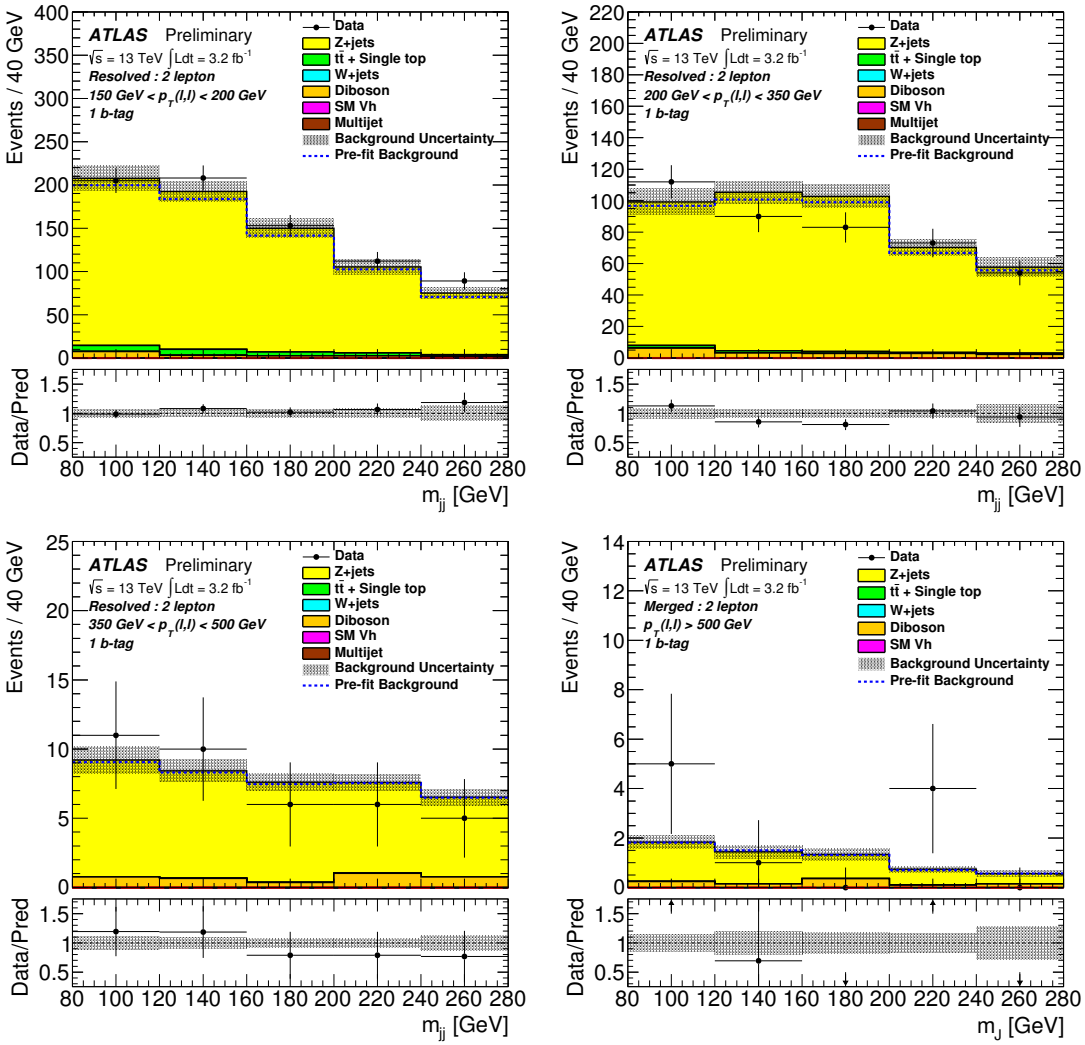

Figure 9: Post-fit plots of the invariant mass of the two signal jets for the 2 lepton control region for 1 tag events.

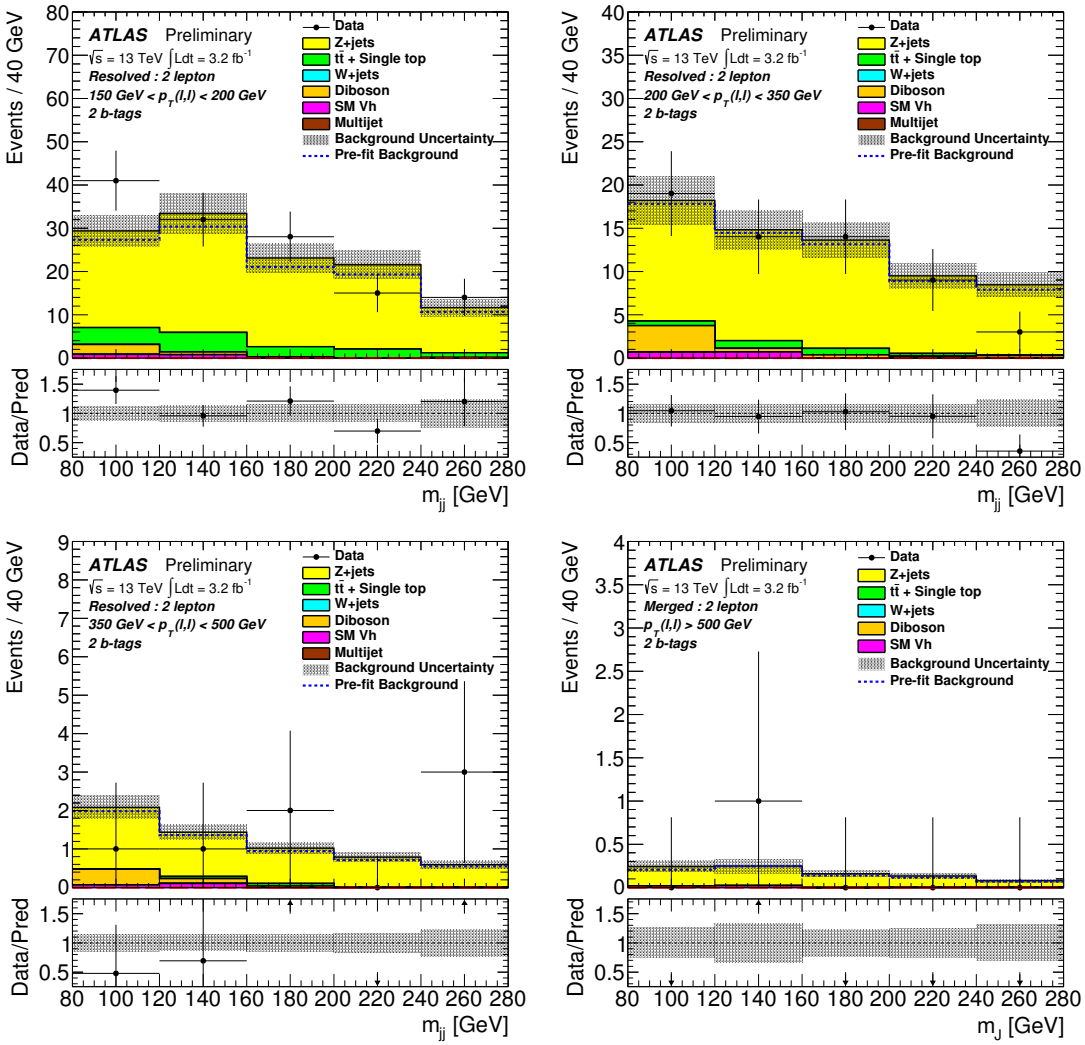

Figure 10: Post-fit plots of the invariant mass of the two signal jets for the 2 lepton control region for 2 tag events.

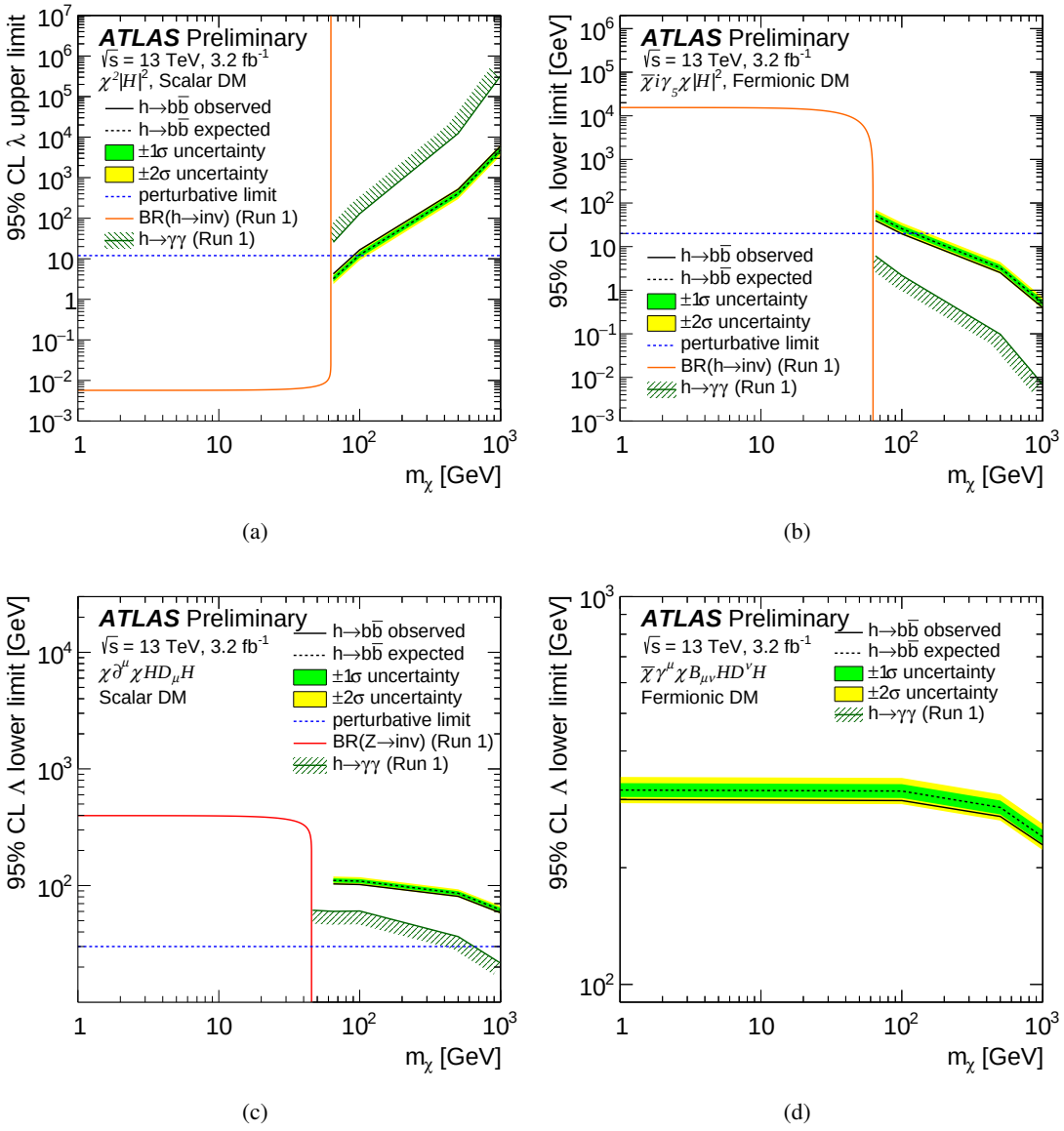

Figure 11: 95% CL upper limits on the coupling strength λ or suppression scale Λ as a function of the DM mass (m_χ) for EFT operators (a) $\chi^2\,|H|^2$, (b) $\bar{\chi}i\gamma_5\chi\,|H|^2$, (c) $\chi^\dagger\partial^\mu\chi H^\dagger D_\mu H$, and (d) $\bar{\chi}\gamma^\mu\chi B_{\mu\nu}H^\dagger D^\nu H$. Solid black lines are due to $h(\rightarrow b\bar{b})$ + $E_{\mathrm{T}}^{\mathrm{miss}}$ (this analysis); regions below the lines are excluded. The solid green line with hash marks indicates regions excluded by the search for $h(\rightarrow \gamma\gamma)$ + $E_{\mathrm{T}}^{\mathrm{miss}}$ (Phys. Rev. Lett. 115 (2015) 131801). The region below the dashed blue line fails the perturbativity requirement, the red line indicates regions excluded by upper limits on the invisible branching ratio (BR) of the Z boson (Phys. Rept. 427 (2006) 257). All of these models are described in Phys. Rev. D89 (2014) 075017 and are generated with MadGraph v1.5.1 with MSTW2008LO PDF set and PYTHIAv8.175 for parton shower and hadronization with the AU2 tune.

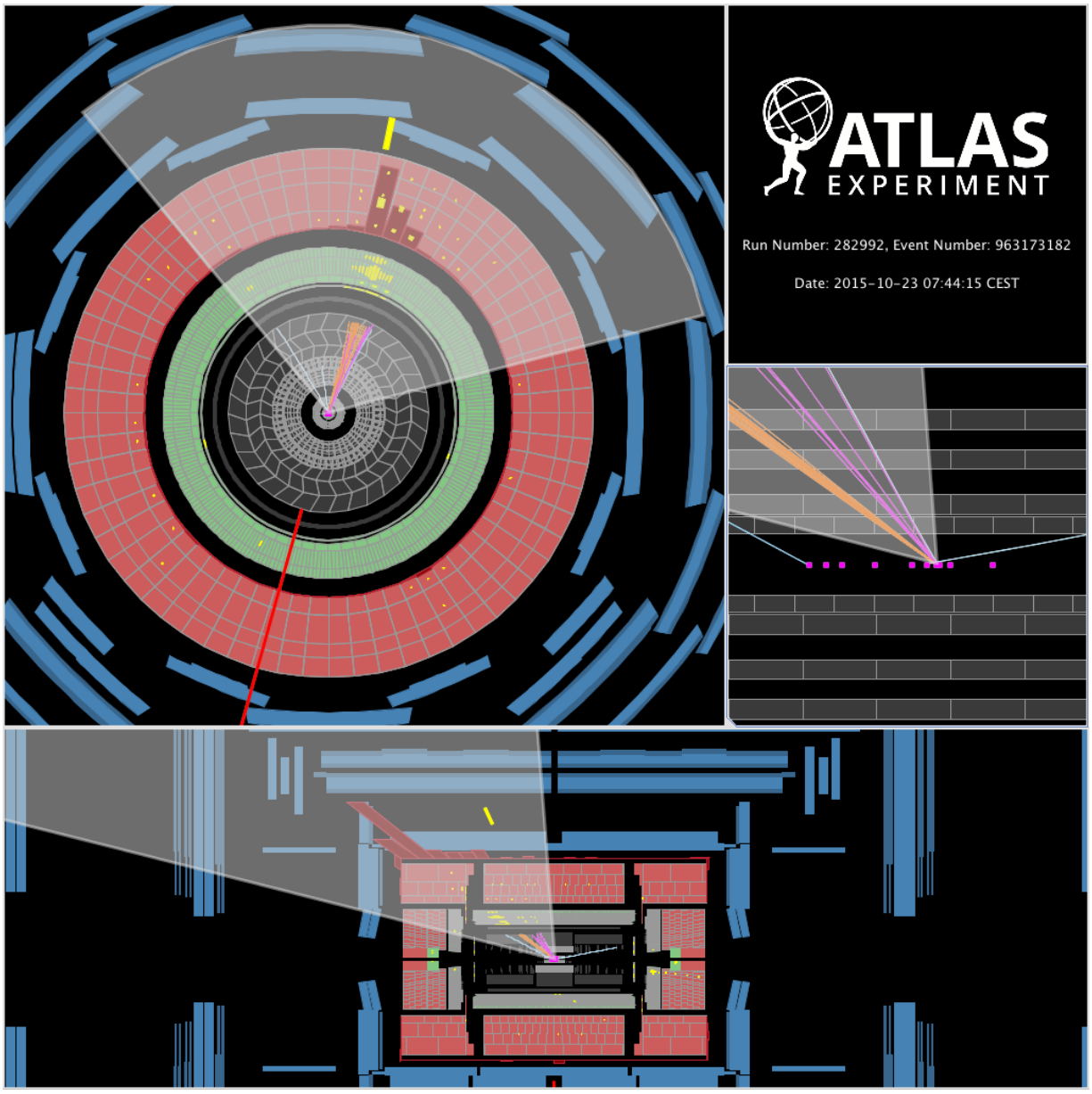

Figure 12: An event display of a signal event in the merged signal region. This event is characterized by $E_{\mathrm{T}}^{\mathrm{miss}}$ =694 GeV and a large-R jet with m_J = 106 GeV and two b-tagged track jets.

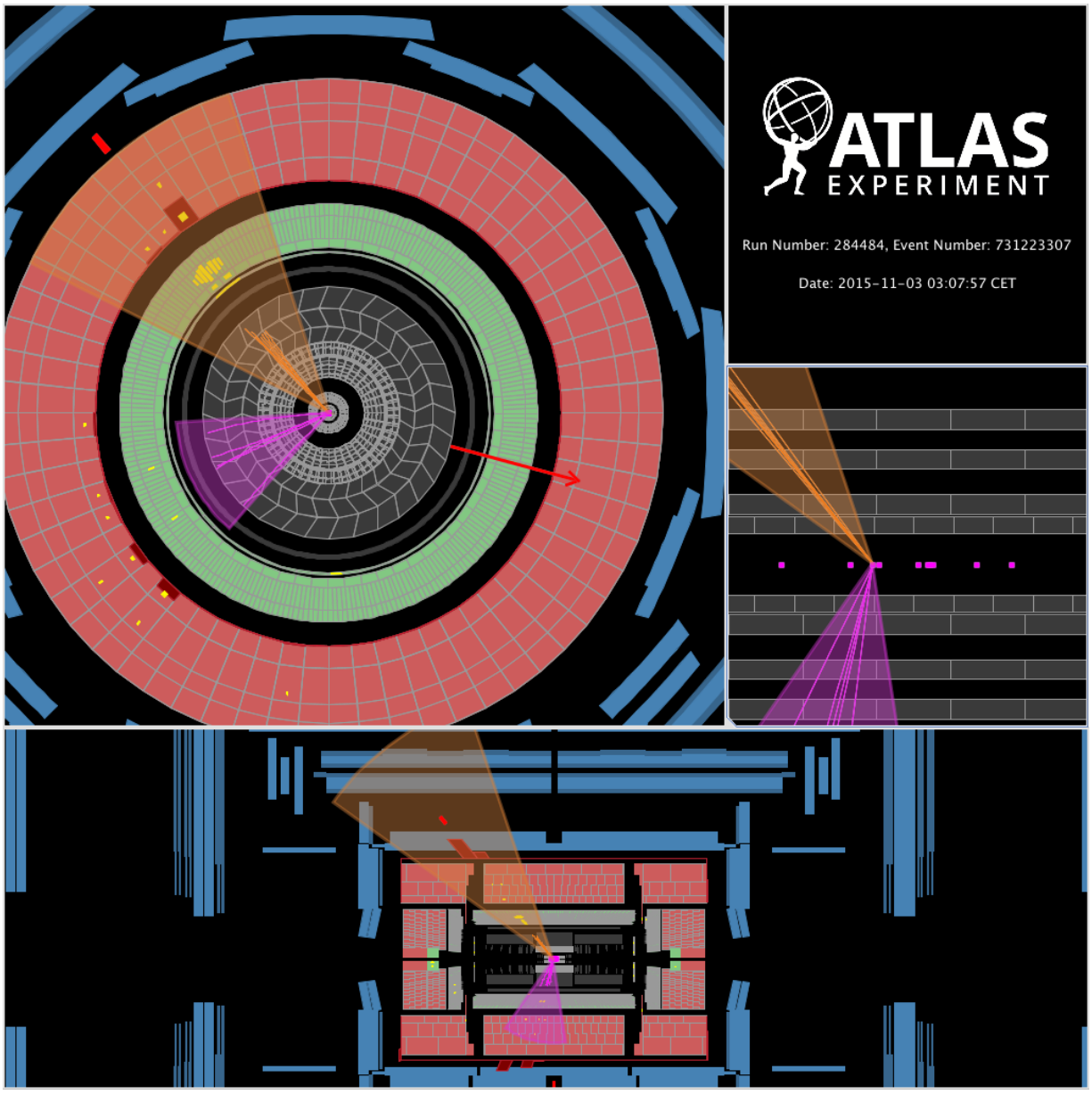

Figure 13: An event display of a signal event in the merged signal region. This event is characterized by $E_{\mathrm{T}}^{\mathrm{miss}}$ =213 GeV and two b-tagged small-R calorimeter jets that form a dijet system with with m_{jj} = 120 GeV.